Small-Signal Modeling of an S-S Compensated IPT System Under Frequency Modulation

Tianqi Li, Guangce Zheng, *Student Member, IEEE*, Chaoqun Qi, Haoyu Wang, *Senior Member, IEEE*, Yu Liu, *Senior Member, IEEE*, and Minfan Fu, *Senior Member, IEEE*

***Abstract*—Frequency modulation is widely utilized in inductive power transfer systems and is also included in the Qi standard for low-power chargers. This brief examines small-signal modeling and simplification methods using an example of an S-S compensated system under frequency modulation. Initially, it develop models for the resonant components under frequency perturbation, which subsequently help in constructing the model of the resonant tank. By incorporating the models of the inverter and rectifier, it derives a sixth-order model for the entire system. The pole-zero analysis helps simplify this sixth-order model to a third-order and a first-order model. Experimental results show that these models can accurately predict the system's control-to-output gain up to 1/2, 2/5, and 1/10 of the switching frequency. These models effectively illustrate the impacts of circuit parameters and the trade-offs between accuracy and complexity.**

***Index Terms*—Inductive power transfer, small-signal model, frequency modulation, S-S compensation.**

I. Introduction

INDUCTIVE power transfer (IPT) systems are widely adopted in various applications, owing to their efficiency and convenience [1], [2], [3]. Especially in charging systems, IPT systems have been used in various application scenes and added many functions to meet the demands of users [4], [5], [6], [7]. Developing small-signal models is crucial for understanding the dynamic behavior of these systems and aiding the design of controllers that ensure performance stability under varying loads and operating conditions. Numerous prior studies have focused on the small-signal modeling of IPT systems operating at steady-state points. These studies have specifically explored the input voltage to output voltage gain for different types of compensation networks employed in these systems [8]. For instance, simple series-series (S-S) compensation has been analyzed extensively in [9], where the focus was on deriving the transfer functions that define the dynamic response of the system during small perturbations. On the other hand, more complex configurations, such as double-sided LCC compensation, have been examined in [10], revealing insights into the trade-offs involved in implementing such designs, particularly regarding efficiency and control stability. To unify these models, a comprehensive model was developed in [11], which integrates the various compensation schemes, enabling a broader perspective on their interactions and performance metrics.

Even for a specific compensation, the modeling process and potential for model simplification can vary significantly, necessitating careful consideration of the specific modulation techniques employed. In addition to the well-known amplitude modulation (AM) [11], alternative strategies such as phase shift modulation (PSM) [12], pulse density modulation (PDM) [13], and frequency modulation (FM) have also proven effective for enhancing the performance of IPT systems. Each of these modulation techniques offers unique advantages and interactions with the resonant tank, which can lead to differing dynamic behaviors and control challenges.

Frequency modulation (FM), in particular, has attracted considerable attention due to its adoption in the Qi standard for low-power chargers, making it a critical component in modern consumer electronics. Although general modulation techniques—such as Generalized State-Space Averaging (GSSA) modeling, discrete-time modeling, and data-driven modeling—have been extensively studied for series-series (S-S) inductive power transfer (IPT) systems, these approaches are typically limited to fixed-frequency operation. Currently, models for FM-based systems have been proposed in [14] and [15]; however, these models are notably complex and are formulated in matrix form, which presents significant challenges for practical implementation. This level of complexity may hinder engineers and system designers from efficiently deploying and optimizing frequency-modulated IPT systems in real-world applications.

This brief develops a small-signal model for an IPT system using FM. Building on the framework of [11], which focuses solely on input voltage perturbation, this brief introduces frequency perturbation into the modeling process. The resonant tank components are analyzed and simplified at the component level to account for frequency variations. The impact of frequency perturbation on both the inverter and rectifier is thoroughly examined. By synthesizing the models of the inverter, resonant tank, and rectifier, a sixth-order model with explicit transfer functions is constructed, facilitating the

Received 27 March 2025; revised 22 May 2025; accepted 18 June 2025. Date of publication 23 June 2025; date of current version 1 August 2025. This work was supported in part by the National Natural Science Foundation of China under Grant 52477013, and in part by the Lingang Laboratory under Grant LG-GG-202402-06-10. This brief was recommended by Associate Editor V. Monteiro. *(Corresponding author: Minfan Fu.)*

Tianqi Li, Guangce Zheng, and Chaoqun Qi are with the School of Information Science and Technology, ShanghaiTech University, Shanghai 201210, China (e-mail: litq2022@shanghaitech.edu.cn; zhenggc@shanghaitech.edu.cn; qicq@shanghaitech.edu.cn).

Haoyu Wang, Yu Liu, and Minfan Fu are with the School of Information Science and Technology and the Shanghai Engineering Research Center of Energy Efficient and Custom AI IC, ShanghaiTech University, Shanghai 201210, China (e-mail: wanghy@shanghaitech.edu.cn; liuyu@shanghaitech.edu.cn; fumf@shanghaitech.edu.cn).

Digital Object Identifier 10.1109/TCSII.2025.3582261

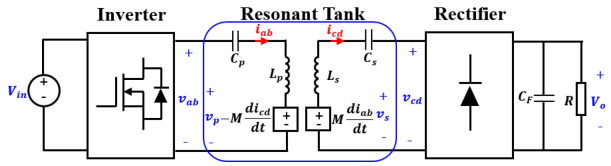

Fig. 1. Topology of an S-S compensated IPT system.

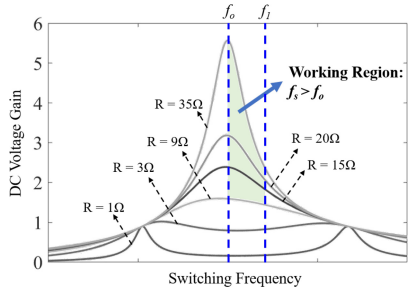

Fig. 2. Gain curve under frequency modulation.

exploration of the trade-offs between model accuracy and complexity. Ultimately, a simplified third-order model and a first-order model are derived and experimentally validated.

II. Small-Signal Modeling and Simplification

A. Frequency Modulation

An S-S compensated IPT system is depicted in Fig. 1. The system comprises an inverter, a resonant tank, and a rectifier. The DC input and output voltages are denoted as V_{in} and V_o, respectively. To ensure stability, a sufficiently large capacitor C_F is employed. The terminal voltages and currents of the resonant tank are represented as v_{ab}, i_{ab}, v_{cd}, and i_{cd}, respectively. The two coils (L_p and L_s) are compensated by capacitors (C_p and C_s). Ideal resonance occurs when the following condition is satisfied:

$$\omega_o L_p - \frac{1}{\omega_o C_p} = \omega_o L_s - \frac{1}{\omega_o C_s} = 0 \tag{1}$$

The system gain curve is depicted in Fig. 2. Typically, the IPT system operates at f_o to ensure a load-independent output current. When the switching frequency exceeds f_o, the gain curve of the IPT system resembles that of the well-known LLC converter. Consequently, FM is commonly adopted in wireless chargers, as indicated in the example working region. The system efficiency is dependent on the switching frequency and load resistance [16].

FM-IPT has been incorporated into the Qi standard and corresponding integrated circuit (IC) designs, and is widely adopted for charging portable electronic devices. Here, a frequency band compatible with the Qi standard is selected for analysis and implementation. To ensure a robust closed-loop design, rather than relying on a trial-and-error approach, a small-signal model is essential. The small-signal model for fixed-frequency systems has been well-explored, and its simplification is largely dependent on the condition in (1). However, when adopting FM, the ideal-resonance assumption becomes invalid, resulting in a significantly more complex model.

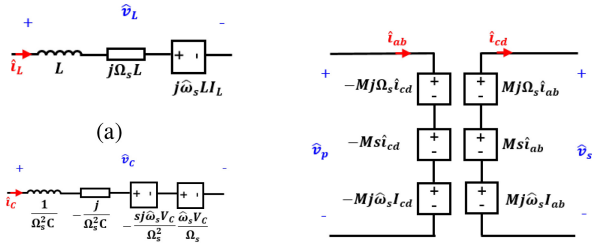

Fig. 3. Small-signal models of resonant components. (a) Inductor. (b) Capacitor. (c) Induced voltage source.

B. Modeling of Resonant Tank

The modeling process of the entire system involves three fundamental steps: modeling each basic component, modeling the complete system, and model simplification. Assuming the system operates at a steady-state frequency Ω_s, the small-signal model must analyze the system response when subjected to a perturbation $\hat{\omega}_s$ is added to Ω_s. The changing rate is described by the observation frequency s. The well-known extended describing function (EDF) method is employed [17]. The primary challenge lies in deriving $\hat{\omega}_s$-dependent component models. The high-order resonant tank significantly contributes to the model complexity.

When operating at $(\Omega_s + \hat{\omega}_s)$, the inductor current i_L with magnitude I_L is generally expressed as

$$i_L = I_L e^{j(\Omega_s + \hat{\omega}_s)t}. \tag{2}$$

Adding perturbation to each variable and substituting (2) into the state equation of an inductor, namely $v_L = L di_L/dt$, yields

$$V_L + \hat{v}_L = sL\left(I_L + \hat{i}_L\right) + j\Omega_s L\left(I_L + \hat{i}_L\right) + j\hat{\omega}_s L\left(I_L + \hat{i}_L\right) \tag{3}$$

After eliminating the steady-state operating terms and neglecting the higher-order perturbation terms on both sides of (3), a process known as linearization, the equation simplifies to:

$$\hat{v}_L = sL\hat{i}_L + j\Omega_s L\hat{i}_L + j\hat{\omega}_s L I_L. \tag{4}$$

This represents the small-signal model of a general inductor under frequency modulation, and the math model can be equivalently described in a circuit manner as shown in Fig. 3(3a).

Similarly, the model of a general capacitor is derived as

$$\hat{i}_C = sC\hat{v}_C + j\Omega_s C\hat{v}_C + j\hat{\omega}_s C V_C. \tag{5}$$

To have the same model form as (4), the capacitor model in (5) is utilized to express $\hat{v}_c$ in terms of $\hat{i}_c$, as shown below:

$$\begin{aligned}\hat{v}_C &= \frac{\hat{i}_C}{sC + j\Omega_s C} - \frac{j\hat{\omega}_s C V_C}{sC + j\Omega_s C} \\ &= \frac{(s - j\Omega_s)\hat{i}_C}{\left(\frac{s^2}{\Omega_s^2} + 1\right)\Omega_s^2 C} - \frac{(s - j\Omega_s)j\hat{\omega}_s C V_C}{\left(\frac{s^2}{\Omega_s^2} + 1\right)\Omega_s^2 C}.\end{aligned} \tag{6}$$

When $s << \Omega_s$, $\frac{s^2}{\Omega_s^2} + 1 \approx 1$, (6) is simplified as

$$\hat{v}_C \approx \frac{s}{\Omega_s^2 C}\hat{i}_C - \frac{j}{\Omega_s C}\hat{i}_C - \frac{sj\hat{\omega}_s V_C}{\Omega_s^2} + \frac{\hat{\omega}_s V_C}{\Omega_s}. \tag{7}$$

Thus, the small-signal model of a capacitor shares the same form as that of an inductor and is shown in Fig. 3(b).

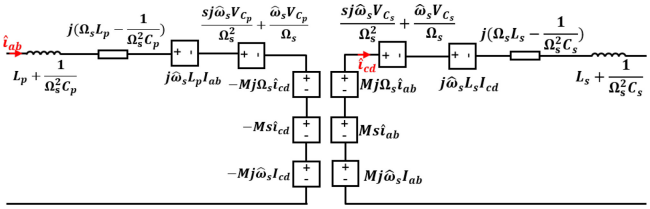

Fig. 4. Small signal model of the resonant tank.

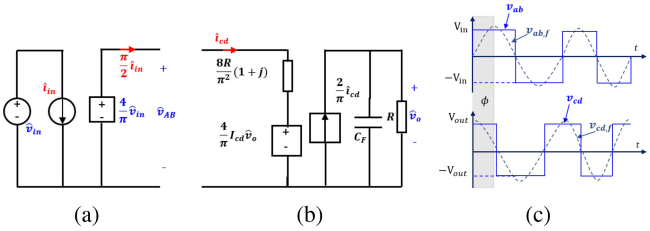

Fig. 5. Small-signal model of inverter and rectifier under AM. (a) Inverter. (b) Rectifier. (c) Terminal waveform.

In the resonant tank, the coil inductor and compensation capacitor can directly apply the conclusions from Fig. 3((a)) and Fig. 3((b)). The voltages induced in the primary and secondary windings, as shown in Fig. 1, follow the equations $v_p = -Mdi_{cd}/dt$ and $v_s = Mdi_{ab}/dt$. Assuming $i_{ab} = I_{ab}e^{j(\Omega_s+\hat{\omega}_s)t}$ and $i_{cd} = I_{cd}e^{j(\Omega_s+\hat{\omega}_s)t}$, the small-signal models for the induced voltage sources are given by:

$$\begin{cases} \hat{v}_p = -Mj\Omega_s\hat{i}_{cd} - Ms\hat{i}_{cd} - Mj\hat{\omega}_s I_{cd} \\ \hat{v}_s = Mj\Omega_s\hat{i}_{ab} + Ms\hat{i}_{ab} + Mj\hat{\omega}_s I_{ab} \end{cases} \tag{8}$$

The above equation could be represented in a circuit format as shown in Fig. 3(c).

After obtaining the component model of the resonant tank, which are given in Fig. 3, the small-signal model of the whole resonant tank is shown in Fig. 4.

C. System-Level Modeling and Simplification

The system-level model requires integrating the models of the inverter, resonant tank, and rectifier. Using the EDF method, the small-signal models of the inverter and rectifier under amplitude modulation (AM) have been presented in [11], as depicted in Fig. 5 (a) and (b). When operating at a nominal frequency Ω_s, a small frequency perturbation $\hat{\omega}$ results in a perturbed operating frequency $\Omega = \Omega_s + \hat{\omega}$. As shown in Fig. 5(c), this perturbation does not alter the magnitude of $v_{ab,f}$, which represents the inverter's fundamental output voltage. Consequently, the AM-based inverter model introduced in [11] remains applicable to frequency modulation (FM) systems by neglecting voltage perturbations. The same approach is valid for modeling the rectifier.

The next step is to combine the models of the inverter, resonant tank, and rectifier. It is advantageous to decompose each subsystem model into two orthogonal components, which facilitates both model synthesis and subsequent calculations. To achieve this decomposition for the resonant tank model shown in Fig. 4, the key idea is to decompose each state variable individually, as discussed in [11]. An example decomposition for the inductor is illustrated in Fig. 6. Once all state

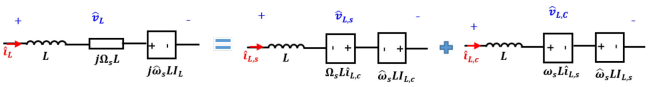

Fig. 6. Orthogonal decomposition of inductor model, i.e., (4).

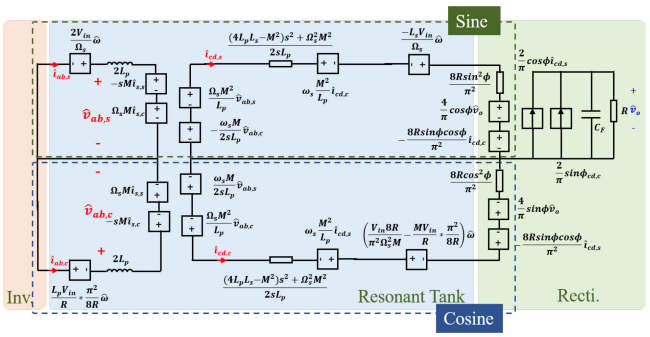

Fig. 7. Sixth-order model of a S-S compensated IPT system.

variables are separated into sine and cosine components, the resonant tank model becomes the central part of Fig. 7.

In the inverter model, the terminal state variables are linearly related by $V_{ab} = \frac{4}{\pi}V_{in}$ and $I_{in} = \frac{2}{\pi}I_{ab}$. Since frequency perturbations do not affect this transformation, the inverter model remains independent of $\hat{\omega}_s$. From a small-signal modeling perspective, steady-state quantities do not explicitly appear, effectively rendering the inverter, which serves as the excitation voltage source, equivalent to a short circuit in the left of Fig. 7.

When using the inverter output voltage as the reference, the rectifier model must account for the phase shift ϕ illustrated in Fig. 5(c). For a symmetrical inductive power transfer (IPT) system, ϕ is given by:

$$\phi = \frac{\pi}{2} - \arctan\left(\frac{\frac{8}{\pi^2}\Omega_s RC_p\left(\Omega_s^2 L_p C_p - 1\right)}{\Omega_s^4 M^2 C_p^2 - \left(\Omega_s^2 L_p C_p + 1\right)^2}\right) \tag{9}$$

Based on Fig. 5(b), its decomposed version appears on the right side of Fig. 7.

After deriving the models of the inverter, resonant tank, and rectifier, the entire system can use the fundamental output voltage of the inverter as the reference. Subsequently, the rest of the circuitry is decomposed into two orthogonal components. This model synthesis approach has been utilized in [11]. The final system model is illustrated in Fig. 7, which leads to a sixth-order control-to-output transfer function as shown below:

$$G_{\omega v} = \frac{\hat{v}_o}{\hat{\omega}_s} = \frac{G_0\left(b_3 s^3 + b_2 s^2 + b_1 s + b_0\right)}{a_6 s^6 + a_5 s^5 + a_4 s^4 + a_3 s^3 + a_2 s^2 + a_1 s + a_0} \tag{10}$$

The coefficients are given in (11) shown at the bottom of the next page .

The sixth-order model is vital for accurately capturing the high-frequency response, particularly when the observation frequency s approaches Ω_s. In the low-frequency domain, a low-order model is generally preferred. To simplify the model, pole-zero analysis is employed. According to control theory, when the real parts of certain poles and zeros are smaller than one-fifth of those of the others, they can be identified as the dominant poles and zeros. These dominant poles and

zeros govern the low-frequency dynamics of the system. By neglecting the high-frequency poles and zeros, the system model can be simplified as:

$$G_{\omega v} = -\frac{R\sin\phi}{\Omega_s V_{in}} \frac{1}{c_3 s^3 + c_2 s^2 + c_1 s + c_0} \tag{12}$$

where the coefficients are defined as:

$$\begin{cases} c_3 = \sin\phi R C_F L_p L_s \\ c_2 = \left(\sin\phi R C_F \pi \sqrt{L_p C_p}/75 + L_p C_p/2\right) \\ c_1 = \pi\sqrt{L_p C_p}/30 + \sin\phi R C_F/5 \\ c_0 = 1/2 \end{cases} \tag{13}$$

The simplified model contains a low-frequency pole and a pair of complex conjugate poles. By further ignoring the effects of the complex conjugate poles, a first-order model is derived as follows:

$$G_{\omega v} = -\frac{R\sin\phi}{\Omega_s V_{in}} \frac{1}{0.5\sin\phi R C_F s + 1} \tag{14}$$

This result indicates that the low-frequency dynamics are primarily influenced by the system's output capacitance C_F.

To balance accuracy and complexity, both high-order and simplified models are developed. The simplified model captures key dynamics and is sufficient for most applications with low bandwidth needs. As all models are linear, controllers remain simple and efficient, with minimal computational burden. The main finding is that frequency modulation mainly impacts the resonant tank, while inverter and rectifier models remain largely unchanged. The modeling approach, starting from resonant elements, can be extended to other typologies.

III. Experiment Verification

An S-S IPT system is constructed to validate the mathematical model, as depicted in Fig. 8. The resonance frequency f_0 is designed at 100 kHz. The system operates with a 15-V input voltage and delivers 30-W output power. The system parameters are provided in Table I. To inject frequency perturbations, the control chip (TI UCC25600) is utilized to realize voltage-controlled oscillation. This chip is originally designed for use in closed-loop controlled LLC converters employing FM. When operated in an open-loop configuration, it is capable of generating a square-wave signal ranging from 40 kHz to 350 kHz by adjusting the input at its RT pin. By sweeping the injected signal, the Bode 100 analyzer can directly measure the control-to-output gain.

At an operating frequency of 104 kHz, the steady-state waveform is illustrated in Fig. 9 (a). Under frequency modulation, another steady-state waveform is shown in Fig. 9 (b) when the frequency is increased to 120 kHz. Within the

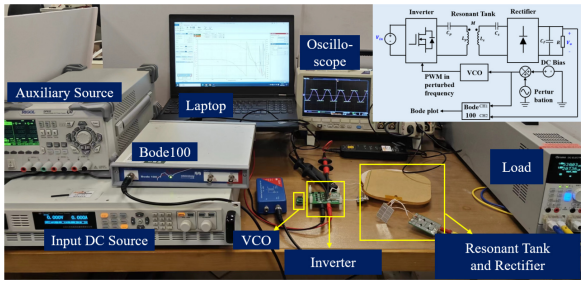

Fig. 8. Experiment setup.

TABLE I
Parameters of the Prototype

f_o	L_p	L_s	C_p
100 kHz	21.5 μH	22.7 μH	108.4 nF
C_s	C_F	M	R
113.6 nF	15.0 μF	12.3 μH	9 Ω

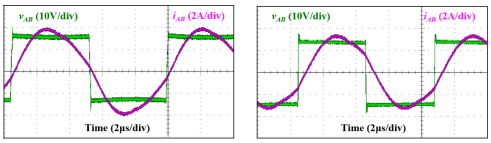

(a) (b)

Fig. 9. Steady-state waveform. (a) $\Omega_s = 104$ kHz. (b) $\Omega_s = 120$ kHz.

$$\begin{aligned}
&G_0 = 8V_{in}R\sin\phi/\pi^4\Omega_s M \quad b_3 = RC_F L_p^2/2\pi^2\Omega_s^6 M^6 \quad b_2 = \pi\left(M^2 + 4L_pL_s\right)/2\Omega_s^3 M^3 \quad b_1 = 8L_p\sin\phi R/\pi^4\Omega_s M \quad b_0 = -1 \\
&a_6 = \sin\phi RC_F\left(M^2 - 4L_pL_s\right)^2/\pi\Omega_s^4 M^4 \\
&a_5 = \left(M^2 - 4L_pL_s\right)\left(2\sin\phi\pi\Omega_s M^2 RC_F - 8\sin\phi\pi\Omega_s L_pL_s RC_F + 16L_pRC_F + 4\pi^2 L_pL_s - \pi^2 M^2\right)/2\pi^2 M^4\Omega_s^4 \\
&a_4 = \left(M^2 - 4L_pL_s\right)\Big(16\sin\phi L_pRC_F\Omega_s + 4\pi^2\Omega_s L_pL_s - \pi^2 M^2\Omega_s - 64\sin\phi\pi RL_p + 4\sin\phi RC_F\pi^2\Omega_s^2 M^2 L_pL_s \\
&\qquad + 2\pi\Omega_s^2 M^4\Big)/2\pi^2 M^4\Omega_s^4 \\
&a_3 = (32\pi\sin\phi RL_p\left(4L_pL_s - M^2\right) + 2\sin\phi RC_F\pi^3 M^2\Omega_s^2\left(L_pL_s + M^2\right) + 16R^2 C_F L_p\Omega_s M^2 + 8\pi^2 L_pL_s\Omega_s M^2 \\
&\qquad + 2\pi^2\Omega_s M^4/\pi^2\Omega_s^3 M^4 \\
&a_2 = \left(16\pi\Omega_s\sin^2\phi R^2 C_F L_p + 8\pi^3\Omega_s L_pL_s + 2\sin\phi\pi^3\Omega_s L_pL_s + 2\pi^3\Omega_s M^2 - 2\sin\phi RC_F\pi^2\Omega_s^2 M^3 - 256L_p\sin\phi R\right)/\pi^3\Omega_s^2 M^2 \\
&a_1 = \left(-2\Omega_s^2\pi^2\sin\phi RC_F M^2 - 256L_p\sin\phi R + \pi^4\Omega_s M^2\right)/\pi^3\Omega_s M^2 \qquad a_0 = \Omega_s\pi
\end{aligned} \tag{11}$$

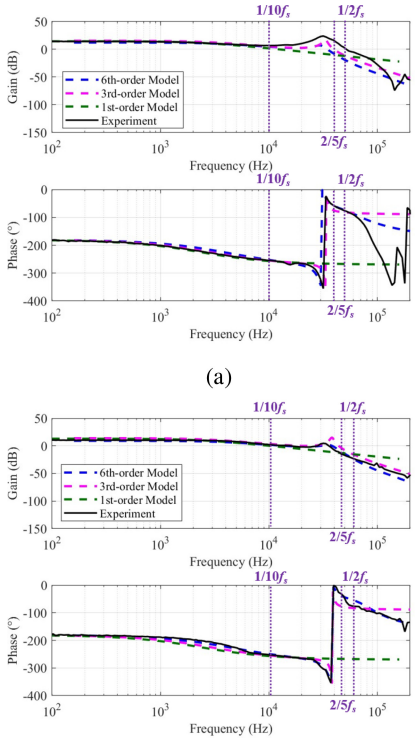

(a)

(b)

Fig. 10. Model verification at frequency domain. (a) $\Omega_s = 104$ kHz. (b) $\Omega_s = 120$ kHz.

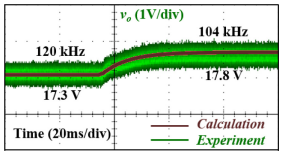

Fig. 11. Dynamic response under step change.

modulation range of 100 kHz to 125 kHz used in consumer electronics, the phase angle ϕ approximates $\frac{\pi}{2}$.

Fig. 10 (a) presents the measured control-to-output gain ($G_{\omega v}$) depicted by the dotted curve when $\Omega_s = 104$ kHz. The measured gain evidently includes high-frequency components due to system non-linearity and high-order resonances. The gain curve, calculated using the sixth-order model, accurately describes the system behavior up to $1/2\Omega_s$. Employing the third-order model, the calculated gain remains precise up to $2/5\Omega_s$, with the presence of a double pole. By further ignoring the effects of the double pole, the first-order model maintains accuracy below $1/10\Omega_s$. These results clearly illustrate the trade-off between model accuracy and complexity. When the switching frequency change to 120 kHz, the derived model is still accurate as shown in Fig. 10 (b).

A step change from 120 kHz to 104 kHz is added on the frequency. The response is shown in Fig.11, which proves the accuracy in the time-domain aspect.

IV. Conclusion

This brief develops a small-signal model for an IPT system using frequency modulation. The model includes frequency perturbation for the resonant tanks, inverter, and rectifier, resulting in a sixth-order transfer function that balances accuracy and complexity. Simplified third-order and first-order models are derived. By building an IPT system using S-S compensation, validation experiments are proceeded on the system and data are collected with Bode100. By comparing the bode plots of mathematical models and IPT system, the frequency-domain and time-domain verification shows the correctness of the models.

References

[1] N. Mirković, L. R. Chamorro, A. Delgado, P. Alou, and M. Vasić, "30 kW bidirectional inductive power transfer charger with intermediate coil for EV applications," *IEEE Trans. Power Electron.*, vol. 39, no. 7, pp. 9007–9024, Jul.2024.

[2] H. Jung and B. Lee, "Wireless power and bidirectional data transfer system for IoT and mobile devices," *IEEE Trans. Ind. Electron.*, vol. 69, no. 11, pp. 11832–11836, Nov. 2022.

[3] K.-S. Yoon, S. Kim, G. Ko, I.-K. Cho, and S. Kim, "Extended ZVS range via LC resonance in current-fed parallel resonant converter for AGV wireless power transfer," *IEEE Trans. Circuits Syst. II, Exp. Briefs*, vol. 72, no. 2, pp. 424–428, Feb. 2025.

[4] Z. Li, G. Ning, K. Zhao, H. Wang, Y. Liu, and M. Fu, "A dual-mode wireless charger based on cascaded rectifier and hybrid compensation," *IEEE Trans. Circuits Syst. II, Exp. Briefs*, vol. 71, no. 3, pp. 1466–1470, Mar. 2024.

[5] A. Mostafa, Y. Wang, F. Lu, and H. Zhang, "Enhanced axial misalignment tolerance in a 10-kw autonomous underwater vehicle wireless charging system utilizing a split solenoid coupler," *IEEE Trans. Power Electron.*, vol. 39, no. 10, pp. 12041–12046, Oct. 2024.

[6] Y. Qu, B. Zhang, W. Gu, J. Li, and X. Shu, "Distance extension of S-PS wireless power transfer system based on parity-time symmetry," *IEEE Trans. Circuits Syst. II, Exp. Briefs*, vol. 70, no. 8, pp. 2954–2958, Aug. 2023.

[7] X. Wang, R. He, Z. Lin, and M. Fu, "Efficiency control for multi-receiver inductive power transfer systems without knowing realtime coupling," *Wireless Power Transf.*, vol. 12, p. e006, Mar. 2025.

[8] H. Feng and S. M. Lukic, "Reduced-order modeling and design of single-stage LCL compensated IPT system for low voltage vehicle charging applications," *IEEE Trans. Veh. Technol.*, vol. 69, no. 4, pp. 3728–3739, Apr. 2020.

[9] Z. U. Zahid et al., "Modeling and control of series–series compensated inductive power transfer system," *IEEE J. Emerg. Sel. Top. Power Electron.*, vol. 3, no. 1, pp. 111–123, Mar. 2015.

[10] G. Zheng, P. Zhao, H. Li, and M. Fu, "Small-signal model of an inductive power transfer system using LCC–LCC compensation," *IEEE Trans. Ind. Appl.*, vol. 58, no. 1, pp. 1201–1210, Jan./Feb. 2022.

[11] G. Zheng, C. Qi, Y. Liu, J. Liang, H. Wang, and M. Fu, "Uniform and simplified small-signal model for inductive power transfer systems," *IEEE Trans. Power Electron.*, vol. 38, no. 2, pp. 2709–2719, Feb. 2023.

[12] J. Lu, S. Sun, H. Ke, and G. Zhu, "Triple phase shift modulation scheme for bidirectional wireless power transfer systems with efficiency maximization," *IEEE Trans. Circuits Syst. II, Exp. Briefs*, vol. 71, no. 12, pp. 5029–5033, Dec. 2024.

[13] H. Li, K. Wang, J. Fang, and Y. Tang, "Pulse density modulated ZVS full-bridge converters for wireless power transfer systems," *IEEE Trans. Power Electron.*, vol. 34, no. 1, pp. 369–377, Jan. 2019.

[14] E. S. Lee, "Frequency-modulation-based IPT with magnetic communication for EV wireless charging," *IEEE Trans. Ind. Electron.*, vol. 70, no. 2, pp. 1398–1408, Feb. 2023.

[15] J. Zhou, S. Chen, G. Guidi, Y. Tang, and J. A. Suul, "Dynamic improvement of sub-resonant frequency control for inductive power transfer systems by coupling estimation and sending-side gain-scheduled control," *IEEE Trans. Ind. Appl.*, vol. 60, no. 2, pp. 3734–3745, Mar./Apr. 2024.

[16] Z. Huang, S.-C. Wong, and C. K. Tse, "Comparison of basic inductive power transfer systems with linear control achieving optimized efficiency," *IEEE Trans. Power Electron.*, vol. 35, no. 3, pp. 3276–3286, Mar. 2020.

[17] E. Yang, F. Lee, and M. Jovanovic, "Small-signal modeling of series and parallel resonant converters," in *Proc. 7th Annu. Appl. Power Electron. Conf. Expo.*, 1992, pp. 785–792.